Revision 1

Word count: 6354

Magmatic degassing controlled the metal budget of the Axi epithermal gold deposit

NUO LI [1,2*], BO ZHANG [3,4], THOMAS ULRICH [5], A.E. WILLIAMS-JONES [4], YANJING CHEN [3]

[1] *Xinjiang Research Center for Mineral Resources, Xinjiang Institute of Ecology and Geography, Chinese Academy of Sciences, Urumqi 830011, China*

[2] *State Key Laboratory of Desert and Oasis Ecology, Xinjiang Institute of Ecology and Geography, Chinese Academy of Sciences, Urumqi 830011, China;*

[3] *Laboratory of Orogen and Crust Evolution, Peking University, Beijing 100871, China*

[4] *Department of Earth and Planetary Sciences, McGill University, 3450 University Street, Montréal, Québec H3A 0E8, Canada*

[5] *Department of Geoscience, Aarhus University, Aarhus DK-8000, Denmark*

*E-mail: Nuo Li, linuo@ms.xjb.ac.cn; nuolipku@126.com

ABSTRACT

From integrated textural and compositional studies of auriferous and barren pyrite/marcasite in the epithermal Axi gold deposit, China, we have identified a relationship between multiple gold mineralizing events, mafic magma recharge and fluid-rock reactions. Three generations of pyrite (Py1–3) and four generations of marcasite (Mar1–4) record episodic gold mineralizing events, followed by silver-copper-lead-zinc-cadmium enrichment. The gold mineralizing events were recorded by high concentrations of sub-nanometer sized gold in Py1, Py3, and Mar3 (max. = 147, 129 and 34 ppm, med. = 39, 34 and 12 ppm). Based on previous Re-Os ages determinations of pyrite and U-Pb zircon ages of the andesitic wallrock, these gold events slightly postdated pulsed mafic magma recharge, and represent the incursion of Au-As-S-rich magmatic volatiles into circulating meteoric water. Silver-Cu-Pb-Zn-Cd enrichment in Py2, Mar2 and Mar4 are consistent with quiescent degassing and gradual Ag-Cu-Pb-Zn-Cd enrichment in an evolved felsic magma. Barren Mar1 records the dominance of meteoric water, and a limited magmatic fluid contribution. High Co-Ni-V-Cr-Ti contents in porous cores of Py1 and Mar2 are attributed to wall rock alteration and dissolution-reprecipitation. The results provide convincing evidence that the metal budget (especially for Au, Ag, Cu, Pb, Zn, Sb) of the hydrothermal fluids and sulfides in epithermal systems is controlled by the influx of magmatic fluids and associated magma, whereas the enrichment of certain

fluid-immobile elements, such as Co, Ni, V, Cr and Ti, is caused in part by fluid-rock interaction.

Keywords: Mafic recharge; magma degassing; metal budget; fluid-rock interaction; epithermal deposit; Axi; Central Asian Orogenic Belt

INTRODUCTION

Andesites play an important role in the formation and evolution of continental crust at convergent margins (Rudnick, 1995). They can be produced through fractional crystallization of basalt and crustal assimilation, slab melting, hydrous melting of peridotite, or magma mixing between mafic and felsic magmas (Carmichael, 2002; Defant and Drummond, 1990; Laumonier et al., 2014; Lee and Bachmann, 2014; Reubi and Blundy, 2009). In the last of these mechanisms, the replenishment of a shallower, felsic and partially solidified magma reservoir by mafic magma yields evolved (andesitic to dacitic), volatile-rich magmas that are of sufficiently low density to erupt (Kent et al., 2010).

Epithermal deposits are commonly associated with volcanic rocks in magmatic arcs (Simmons et al., 2005). Notwithstanding the debate concerning the nature of the magmatic contribution to the epithermal mineralization, it has been proposed that the characteristics of epithermal ore-forming systems, as well as those of analogous geothermal systems, are mainly determined by the nature of the associated magmatism (Giggenbach, 1995; Sillitoe and Hedenquist, 2003; Simmons and Brown, 2007). Considering that mafic melt is intrinsically rich in gold and sulfur (Hattori and Keith, 2001; Nadeau et al., 2016), the question arises: Does mafic magma replenishment and the mixing of mafic magma with felsic magma at mid-crustal levels affect the upper-crustal epithermal mineralization?

We selected the Axi epithermal gold deposit (>70 t Au; Chen et al., 2012), NW China (Fig. 1), to provide the context in which to answer this question because it has been clearly shown that the host andesitic rocks were the products of episodic mafic magma injection and mixing with shallower felsic magmas (Zhang, 2020). Moreover, detailed geochronologic studies demonstrate that precipitation of auriferous pyrite (at ca. 355 Ma and 332 Ma, Re-Os isochron, Liu et al., 2020; Li et al., 2022) slightly postdated mafic magma injection (351−357 Ma and 340 Ma, zircon U-Pb age, Li et al., 2022), indicating a potential link between mafic magma replenishment and gold mineralization.

In this paper, we report the results of combined textural and *in situ* trace-element studies of auriferous and barren pyrite/marcasite. These results reveal how mafic magma intrusion, magma mixing, and fluid-rock interaction affect metal budgets in epithermal systems.

THE AXI VOLCANICS AND GOLD MINERALIZATION

The Axi district is located in the Chinese Western Tianshan in an area of long-lived, subduction-related arc magmatism (Yu et al., 2018; Ye et al., 2020). The deposit is hosted by volcanic-sedimentary rocks of the Late Paleozoic Dahalajunshan

Formation (Fig. 1). Volcanism began at ca. 410 Ma and focused in the vicinity of the Axi deposit from 361 to 340 Ma (Li et al., 2022 and references therein). The volcanics exposed in the deposit consist of crystal-rich (30–50%) andesitic to dacitic rocks in which plagioclase, clinopyroxene, amphibole and quartz phenocrysts are embedded in a microcrystalline groundmass of plagioclase, magnetite and ilmenite. A wealth of petrological and geochemical evidence shows that magma mixing played an important role in the petrogenesis of the Axi volcanics, including the development of disequilibrium textures (e.g., inverse zoning, patchy zoning, sieve textures) involving plagioclase phenocrysts, the resorption of quartz phenocrysts, the entrapment of quenched mafic and felsic silicate melt inclusions by quartz phenocrysts and the changes in bulk rock chemistry that led to simple linear trends on bivariate plots of major oxide components (Zhang, 2020).

Nearly 90% of the gold (ca. 60 tonnes, with an average grade of 5.6 g/t) were mined from the No. 1 orebody (Rui et al., 2002; Chen et al., 2012). As details of the alteration and mineralization have been reported by Zhai et al. (2009), An and Zhu (2018); Liu et al. (2018, 2020), and Zhang et al. (2018), only a brief summary of these features is presented below.

The hydrothermally altered rock contains quartz, chalcedony, calcite, sericite and adularia (Bao et al., 2002; Zhai et al., 2009), an assemblage typical of low sulfidation epithermal deposits (White and Hedenqueist, 1990, 1995; Simmons et al., 2005). A zonal distribution of alteration is observed, from an inner silicification zone outwards through adularia-sericite to propylitic alteration zones. Silicification is most closely associated with gold mineralization. The adjacent adularia-sericite alteration zone comprises sericite, quartz, adularia, plus minor illite and carbonate (Zhai et al., 2009; An and Zhu, 2018; Liu et al., 2020). The peripheral propylitic alteration is characterized by the mineral assemblage chlorite, carbonate, and epidote. Native gold, electrum, pyrite, marcasite, sphalerite, chalcopyrite, tetrahedrite and galena are the main ore minerals (Liu et al., 2018; Zhang et al., 2018).

SAMPLING AND ANALYSIS TECHNIQUES

Sampling

Over 500 samples from outcrop and eight drill holes (ZK2404, ZK2405, ZK4811, ZK3605, ZK3507, ZK4002, ZK4004, ZK4007) were examined petrographically in order to identify key minerals and textures. Twelve representative pyrite and marcasite samples from drill holes ZK2404 and ZK2405 were selected for further study.

SEM-BSE imaging

Thin sections were prepared and examined using transmitted and reflected light microscopy to characterize the morphology, textures and paragenesis of pyrite and marcasite. This was followed by SEM-BSE imaging using a FEI Quanta 650 FEG scanning electron microscope (SEM) at the Key Laboratory of Orogenic Belts and Crustal Evolution, Peking University. The SEM is equipped with an energy dispersive spectrometer (EDS), which allows combined backscattered electron (BSE) imaging of

DOI: https://doi.org/10.2138/am-2022-8610. http://www.minsocam.org/

mineral morphology and compositional analysis. The applied voltage was 10 to 20 kV, with a spot-size of 4.0 to 5.0 μm, and a dwell time of 20 to 30 μs.

LA-ICPMS trace element analyses

The trace element composition of the sulfide minerals was analyzed using laser-ablation inductively coupled plasma mass spectrometry (LA-ICPMS) at the Aarhus Geochemistry and Isotope Research platform (AGiR), Department of Geoscience, Aarhus University, Denmark. A 193 nm ArF Excimer laser from Resonetics attached to an Agilent 7900 ICPMS was used for this purpose. The ablation rate was 8 Hz and the laser energy was 70 mJ. Helium was used as the carrier gas, which was mixed with Ar before it entered the ICP. A total of 245 single-spot analyses were performed using a laser beam that varied from 6 to 60 μm, depending on the size of the crystals. All the data were collected in time-resolved mode. The analysis time was 55 seconds, including an initial 25 seconds of background measurement and 30 seconds of ablation. Data for a set of 20 elements were reported for the spot analyses (Hg, Au, Sb, Ag, Mo, Se, As, Zn, Cu, Co, Mn, Cr, V, Cs, Tl, Pb, Sc, Ti, Ni and Al). Bismuth, Sn, In, Cd, Pt and U were also analyzed, but their concentrations were typically very low (<1 ppm) and in many cases below the limit of detection.

The NIST 610 synthetic glass and MASS 1 pressed sulfide reference materials were used as external calibration standards. The reproducibility and accuracy of MASS-1 for different analytical sessions are given in Table A1. The relative standard

DOI: https://doi.org/10.2138/am-2022-8610. http://www.minsocam.org/

deviation for the different elements is between 2 − 10% (Table A1). The standards were analyzed after roughly every 10th pyrite analysis. For the quantification of the data, the Fe concentration obtained by electron microprobe analysis (Zhang et al., 2018) was used as the internal standard. The data processing and quantification were done using Iolite software (Paton et al., 2011).

In order to develop a chemical profile across selected pyrite grains, two LA-ICPMS line scans were conducted. The sample was moved under the laser along a line, crossing the mineral grain at a scanning speed of 8 μm/s with a spot size of 8 μm. The elements mentioned above were chosen for these analyses. The profiles varied between 300 to 400 μm in length.

RESULTS

Types of pyrite/marcasite

Previous studies have documented many features of the pyrite at Axi, including their textures, paragenetic relationships and composition (Zhang et al., 2018; Liu et al., 2015, 2018). These studies reveal that pyrite hosts nearly half of the total gold reserve, and that there are three generations of pyrite. In this study, we couple detailed SEM/EDS imaging of pyrite and marcasite with specific textures/minerals, including crustiform banding, hydrothermal breccias, adularia, platy calcite/quartz and replacement textures, and use them to refine previous textural and mineralogic interpretations.

The earliest pyrite, Py1 (50 − 1500 μm in diameter, Fig. 2, 3) is associated with quartz and sericite. It comprises a corroded, porous core (Py1a), a compact, inclusion-free mantle (Py1b), an oscillatory-zoned rim (Py1c), and an arsenopyrite overgrowth (these features are not present in all the crystals). The anhedral Py1a replaced clinopyroxene phenocrysts as pseudomorphs (Fig. 3B) or is concentrated close to the fluid-rock reaction front (Fig. 3C). Subhedral to euhedral Py1b and Py1c are more common in quartz-dominated cements or veinlets and away from the fluid-rock reaction front (Fig. 3C). Anhedral Py2 (50 − 1000 μm in diameter) coexists with chalcopyrite, sphalerite, tetrahedrite, quartz, calcite and chlorite (Fig. 2B, 3D). Tiny Py3 crystals (10 − 50 μm in diameter) are euhedral to subhedral, and oscillatory-zoned (Fig. 2C). They are surrounded by chalcedony ± calcite, and cement Py1 and/or Py2 clasts in breccias (Fig. 3F).

In addition to pyrite, we identified four generations of marcasite (Figs. 2-4) at shallower depth (< 280 m) than pyrite (that is present to 720 m). The blade-shaped Mar1 (50 − 600 μm in length) coexists with fine- to coarse-grained quartz, chalcedony and/or calcite. It may crosscut Py1 (Fig. 3A) and Py2 and hence crystallized later than them. This marcasite occurs in crustiform layers with a rhythmic alternation of quartz, chalcedony, Py3 and Mar1 (Fig. 4). Since Py3 occurs more commonly in the outer layers, and Mar1 in the inner layers, we propose that Mar1 crystallized contemporaneously with or slightly later than Py3. The second marcasite generation, Mar2, forms radial or fan-shaped aggregates (100 − 2000 μm in length) and has an inclusion-rich, porous core (Mar2a) that is surrounded by a homogeneous marcasite overgrowth (Mar2b) and arsenopyrite (Fig. 2D). It cements hydrothermal breccia fragments together with fine-grained quartz, chalcedony and minor calcite. This generation of marcasite was followed by Mar3 (100 − 1500 μm in length) in calcite± chalcedony veins/cements. Commonly, Mar3 crosscuts anhedral Py2 (Fig. 3E), or cements breccia clasts containing earlier pyrite and marcasite generations. Locally, Mar3-calcite veins crosscut lattice structures and adularia, and calcite may fill the lattice interstices (Fig. 3I). The latest marcasite generation (Mar4) forms acicular crystals/aggregates (50 −1000 μm in length) and is hosted by calcite veins, in which the calcite is euhedral to subhedral and occurs as rhombs with alternating clear and "dusted" zones due to sub-microscopic inclusions. These veins crosscut calcite-chalcedony-Mar3 veins (Fig. 3H), indicating that Mar4 was later than Mar3. On a modal basis, Py1, Py3, Mar2 and Mar3 are the most abundant pyrite and marcasite phases, followed by minor Py2, and traces of Mar4 and Mar1.

The trace element record of episodic mineralization

The trace element data for pyrite and marcasite are summarized in Table 1 and listed in Appendix A2. In the following text, the maximum (max.) values are reported for gold hosted by Py1b, Py3 and Mar3, and median (med.) values are reported for all other elements/samples (see also Fig. 5).

The compositional data reveal episodic gold mineralizing events. Each of these events was followed by a period of silver and base metal enrichment. The first gold

DOI: https://doi.org/10.2138/am-2022-8610. http://www.minsocam.org/

mineralizing event is recorded by Py1b that has the highest concentrations of Au (max. = 147 ppm, med. = 39 ppm) and As (67500 ppm). The precursor Py1a, by contrast, is characterized by higher Co (209 ppm), Ni (510 ppm), V (14 ppm), Cr (12 ppm) and Ti (3300 ppm) contents than Py1b (Co = 25 ppm, Ni = 35 ppm, V = 0.83 ppm, Cr = 3.5 ppm, Ti = 12 ppm). The compositional variation of different parts of Py1 crystals is clearly illustrated by the laser ablation traverses across a Py1 grain (Fig. 6). The subsequent Py1c is relatively deficient in most trace elements in comparison to Py1a and Py1b, especially As (15000 ppm), Zn (1.1 ppm), Cu (96 ppm), Co (11 ppm), V (0.67 ppm), Cr (1.0 ppm) and Ti (7.7 ppm). Gold mineralization was followed by the introduction of Cu, Pb, Zn and Sb, which is recorded in Py2 (Cu = 928 ppm, Pb = 124 ppm, Zn = 96 ppm, Sb = 884 ppm). This pyrite type has the highest concentration of Ag among all the samples (max. = 305 ppm, med. = 157 ppm) but is depleted in Au (6.0 ppm).

The second gold mineralizing event is documented by the composition of Py3 (max. = 129 ppm, med. = 34 ppm Au). Later Mar1, however, is depleted in most trace elements. A second period of Ag-Zn enrichment is recorded by Mar2 (containing 243 ppm Ag and 69 ppm Zn in the core, and 60 ppm Ag and 27 ppm Zn in the rim). Its porous core (Mar2a) has higher Co (298 ppm), Ni (697 ppm), V (9.7 ppm), Cr (8.0 ppm) and Ti (32 ppm) contents than the compact Mar2b overgrowth (Co = 58 ppm, Ni = 195 ppm, V = 7.0 ppm, Cr = 3.8 ppm, Ti = 13 ppm), mimicking the compositional difference between Py1a and Py1b (Fig. 5).

DOI: https://doi.org/10.2138/am-2022-8610. http://www.minsocam.org/

A weak gold mineralizing event may be indicated by the composition of Mar3, although its Au content is much lower (max.= 34 ppm, med. = 12 ppm) than those of Py1b (39 ppm) and Py3 (34 ppm). It also has relatively high Ag (146 ppm), Pb (169 ppm), Zn (29 ppm) and Sb (872 ppm) contents. The youngest marcasite variety, Mar4, is characterized by extremely low contents of Au (0.11 ppm), Ag (13 ppm) and As (3115 ppm), but moderately high Pb (1027 ppm), Zn (104 ppm) and Sb (417 ppm) contents.

INTERPRETATION AND DISCUSSION

In a previous study, we showed that the Axi andesites accumulated incrementally through injections of mafic magma into a shallow, felsic magma reservoir (Li et al., 2022). We documented the injection events by the textural features of zircon in which an anhedral, antecrystic core is resorbed and embayed by a thin, irregular zone (<5 μm) prior to overgrowth by an oscillatory-zoned autocrystic rim (Li et al., 2022). Using the ages of the core and rim of the zircon, the main period of injections is interpreted to have been between 351 and 357 Ma, contemporaneous with the crystallization of Py1b (357 ± 18 Ma, 353 ± 6 Ma, Re-Os isochron, Liu et al., 2020; Li et al., 2022). This chronology, in combination with our new sulfide trace element data, provides compelling evidence for a link between magma injection and gold mineralization. We propose that fluid exsolution associated with mafic magma injections and interspersed periods of magma quiescence exerted a first-order control on the metal budget of the ores (Fig. 7). We further propose that enrichment of certain fluid-immobile elements, such as Co, Ni, V, Cr and Ti, was caused, in part, by fluid-rock interaction. A detailed discussion is provided below.

The earliest pyrite, anhedral Py1a, is interpreted to have formed as a result of fluid-mediated sulfidation, or coupled dissolution-reprecipitation reactions (Putnis, 2009), based on the observation that it replaced clinopyroxene phenocrysts as pseudomorphs, or is concentrated close to the sharp fluid-rock reaction front (Fig. 3C). Intense alteration led to the breakdown of clinopyroxene, amphibole, plagioclase, magnetite-ilmenite and other constituents of the andesite host. Consequently, elements that were once compatible in these phases (such Co, Ni, V, Cr and Ti) were released into the circulating fluids (Mustard et al., 2006; Jenner et al., 2010), and were scavenged by the alteration products. Thus, it was the alteration of the parent mineral, coupled in space and time with the precipitation of daughter minerals and co-generation of porosity, that led to the development of porous, Co-Ni-V-Cr-Ti-rich Py1a.

The gold mineralization event recorded by Py1b is interpreted to have been associated with mafic magma intrusion into the shallow, felsic magma reservoir referred to above. Although the sulfur and gold contents of igneous rocks in the Axi area have not been analyzed, mafic magma is generally considered to have high sulfur (more than several thousand ppm; Nadeau et al., 2016) and Au contents (Keith et al., 1997; Hattori and Keith, 2001; Halter et al., 2005; Stern et al., 2007; Zajacz et al., 2012; Guo and Audetat, 2017), and thus, is likely to have been the source of sulfur and gold. Injections of mafic magma would have induced a sudden over-saturation in volatiles (Kent et al., 2010; Nadeau et al., 2016), with sulfur partitioning preferentially into the exsolving supercritical fluid (a $D_S^{fluid/melt}$ value of 20 has been proposed based on hydrothermal S partitioning experiments, Webster and Botcharnikov, 2011). Elements such as Au, As and Hg are readily transported by aqueous vapor, as shown by the compositions of volcanic gases and their sublimates (Williams-Jones and Heinrich, 2005). This reflects the high volatility of Hg and As (Williams-Jones et al., 2002); and Au prefers reduced sulfur, which also partitions preferentially into the vapor (Hurtig and Williams-Jones, 2014; Williams-Jones and Migdisov, 2014). In contrast, elements such as Pb and Zn are likely to have low volatility because of the very strong bonds that they form with chloride ions in aqueous liquids. On rising above the depth of exsolution, the supercritical fluid, which would have been liquid-like because of the high temperature of the mafic magma, would have condensed a small proportion of brine and Au-As-S would have been transported upwards dominantly by the more buoyant vapor. Incursion of this Au-As-S-rich vapor thus would have greatly increased the gold content of the circulating meteoric fluids and decreased their pH (Zhai et al. 2009), leading to gold mineralization and associated quartz-sericite-pyrite (Py1b) alteration. Later Py1c is interpreted to have precipitated from fluids with lesser inputs of magmatic components, and thus less Au and As.

The Ag and base metal-rich Py2 postdated Py1 (Liu et al., 2020; Zhang et al., 2018) and the related mafic magma injection. It possibly accompanied a period of magma quiescence, during which there was a gradual enrichment of Ag, Cu, Pb, Zn and Sb in the evolved magma and exsolved fluids (Nadeau et al., 2016). In the absence of mafic magma injection, the supercritical fluid would have been liquid-like because of its lower temperature, and would have separated to produce a small proportion of vapor leaving a brine more enriched in Cl (Giggenbach, 1997; Zajacz et al., 2008). This, in turn, would have enhanced the transportation of Cl-complexed elements (such as Ag, Cu, Pb, Zn and Sb, Wood and Samson, 1998; Seward et al., 2014) into shallow meteoric water. As a representative of the second gold mineralizing event, Py3 incorporated comparable amounts of Au and As to Py1b, indicating a similar source, i.e., mafic magma. The concentrations of Ag, Cu, Pb, Zn and Sb in Py3, however, are slightly higher than those of Py1b. Invoking a contribution from the felsic magma would reconcile this issue, by providing an additional metal reservoir for Ag, Cu, Pb, Zn and Sb. The deposition of Py3 is attributed to fluid boiling, as shown by: (1) the development of hydrothermal breccias (with Py3 ± chalcedony as the cement); and (2) the occurrence of adularia and bladed calcite (pseudomorphed by quartz) (Fig. 3I). Boiling not only caused precipitation of gold, bladed calcite and adularia (Simmons et al., 2005), but fractured the surrounding rocks, accelerating mixing with meteoric fluids. Marcasite has been shown to form from aqueous solutions with a pH < 5, at temperatures of 80 – 240 °C, in the presence of H_2S_2 (aq) (Murowchick, 1992), whereas Py3 is interpreted to have deposited at 325 – 385 °C, as determined by the arsenopyrite geothermometer (Zhang et al., 2018). The occurrence of Py3 and Mar1 in alternating crustiform layers (Fig. 4) may have been the result of fluid mixing, with the high temperature, Au-rich Py3 recording a greater magmatic fluid contribution and the low temperature, trace-element-poor Mar1 recording the predominance of meteoric water and a minor magmatic fluid component.

The marcasite variety, Mar2a, shares textural (porous) and compositional (Co-Ni-V-Cr-Ti-rich) characteristics similar to Py1a. The compact overgrowth contains proportions of Ag, Pb, Zn and Sb overlapping with or slightly lower than those of Py2, suggesting a similar metal control by quiescent degassing. Thus, the conditions of formation of Mar2a and Mar2b were comparable to those of Py1a and Py1b, with the exception that the invading fluid was Pb-Zn-Sb-rich instead of Au-As-S-rich. Crystallization of Mar2 was followed by that of Mar3, which contains slightly less Au and As than Py1b and Py3 and may record a small injection of mafic magma that was not identified by zircon age dating. The elevated Ag, Sb and Zn contents suggest a hybrid input involving a contribution from the evolved felsic magma. In the final variety of marcasite, Mar4, the fingerprint of the mafic magma is absent, and only that of the felsic magma (high Pb, Zn and Sb) is recorded.

CONCLUSION AND IMPLICATION

The present work provides convincing evidence for a linkage between mafic recharge, andesite formation and epithermal gold mineralization. It suggests that the bulk metal budget (especially for Au, Ag, Cu, Pb, Zn, Sb) of an epithermal system is controlled primarily by the composition of the fluids, which, in turn, is controlled by the nature of the magma in a shallow magma chamber (Keith et al., 2018; Martin et al., 2020). The episodic gold mineralizing events are attributed to repeated mafic magma injections into a shallow, felsic magma chamber and associated magma degassing. Silver-Cu-Pb-Zn-Sb enrichment, by contrast, is related to quiescent degassing of the felsic magma. It also acknowledges that fluid-rock interaction would have involved coupled dissolution and reprecipitation and facilitated immobile element enrichment such as Co, Ni, V, Cr and Ti. Considering that mafic magma replenishment and its mixing with felsic magma play an important role in the formation of andesite (Anderson, 1976; Eichelberger, 1978; Reubi et al., 2009; Kent et al., 2010), the metal budget reported for Axi may also apply to similar cases in convergent margins.

ACKNOWLEDGMENTS

We are grateful to David Dolejs for the editorial handling and two anonymous reviewers for thoughtful comments that greatly improved the quality of the manuscript. We also thank Dr. Yu Jie, Wu Yanshuang, Chen Xi for assistance in field work. The research was funded by National Natural Science Foundation of China (No. 42122014), the Xinjiang Key Research Project (No. 2021A03001-2) and the

Xinjiang Outstanding Youth Scientific Grant (No. 2020Q006). N. Li acknowledges the Alexander von Humboldt Foundation for support.

REFERENCES CITED

An, F., Zhu, Y.F. (2018) Geology and geochemistry of the Early Permian Axi low-sulfidation epithermal gold deposit in North Tianshan (NW China). Ore Geology Reviews, 100, 12–30. doi.org/10.1016/j.oregeorev.2017.03.021

Anderson, A.T. (1976) Magma mixing: Petrological process and volcanological tool. Journal of Volcanology and Geothermal Research, 1, 3–33. doi.org/10.1016/0377-0273(76)90016-0.

Bao, J.X., Chen, Y.J., Zhang, Z.J., Chen, H.Y., and Liu, Y.L. (2002) The preliminary study of laumontitization of Axi gold deposit and paleogeothermal minerogenetic fluid system in west Tianshan. Acta Scientiarum Naturalium Universitatis Pekinensis, 38, 253–259 (in Chinese with English abstract).

Carmichael, I. S. (2002) The andesite aqueduct: perspectives on the evolution of intermediate magmatism in west-central (105–99°W) Mexico. Contributions to Mineralogy and Petrology, 143, 6, 641–663. doi.org/10.1007/s00410-002-0370-9.

Chen, Y. J., Pirajno, F., Wu, G., Qi, J. P., and Xiong, X. L. (2012) Epithermal deposits in North Xinjiang, NW China. International Journal of Earth Sciences, 101, 889–917. doi.org/10.1007/s00531-011-0689-4.

Defant, M. J., and Drummond, M. S. (1990) Derivation of some modern arc magmas by melting of young subducted lithosphere. Nature, 347, 6294, 662–665. doi.org/10.1038/347662a0.

Eichelberger, J.C. (1978) Andesitic volcanism and crustal evolution. Nature, 275, 21–27. doi.org/10.1038/275021a0.

Giggenbach, W. F. (1995) Variations in the chemical and isotopic composition of fluids discharged from the Taupo volcanic zone, New-Zealand. Journal of Volcanology and Geothermal Research, 68, 89–116. doi.org/10.1016/0377-0273(95)00009-J.

Giggenbach, W.F. (1997) The origin and evolution of fluids in magmatic-hydrothermal systems. In: Barnes, H.L. (eds) Geochemistry of hydrothermal ore deposits. John Wiley & Son, New York, 737–796.

Guo, H.H., Audetat, A. (2017) Transfer of volatiles and metals from mafic to felsic magmas in composite magma chambers: An experimental study. Geochmica et Cosmochimica Acta, 198, 360–378. doi.org/10.1016/j.gca.2016.11.029.

Halter, W.E., Heinrich, C.A., and Pettke, T. (2005) Magma evolution and the formation of porphyry Cu-Au ore fluids: Evidence from silicate and sulfide melt inclusions. Mineralium Deposita, 39, 845–863. doi.org/10.1007/s00126-004-0457-5

Hattori, K. H., and Keith, J. D. (2001) Contribution of mafic melt to porphyry copper mineralization: evidence from Mount Pinatubo, Philippines, and Bingham

Canyon, Utah, USA. Mineralium Deposita, 36, 799–806. doi.org/10.1007/s001260100209.

Hurtig, N.C., and Williams-Jones, A.E. (2014) An experimental study of the solubility of MoO_3 in aqueous vapour and low to intermediate density supercritical fluids. Geochmica et Cosmochimica Acta, 136, 169–193. doi.org/10.1016/j.gca.2014.03.043

Jenner, F.E., O′Neill, H.S.C., Arculus, R.J., Mavrogenes, J.A. (2010) The magnetite crisis in the evolution of arc-related magmas and the initial concentration of Au, Ag and Cu. Journal of Petrology, 51, 2445–2464. doi.org/ 10.1093/petrology/egs015.

Keith, J., Whitney, J., Hattori, K., Ballantyne, G., Christiansen, E., Barr, D., Cannan, T., and Hook, C. (1997) The role of magmatic sulfides and mafic alkaline magmas in the Bingham and Tintic mining district, Utah. Journal of Petrology, 38, 1679–1690. doi.org/10.1093/petrology/38.12.1679

Keith, M., Haase, K. M., Klemd, R., Smith, D. J., Schwarz-Schampera, U., and Bach, W. (2018) Constraints on the source of Cu in a submarine magmatic-hydrothermal system, Brothers volcano, Kermadec island arc. Contributions to Mineralogy and Petrology, 173, 5, 40. doi.org/10.1007/s00410-018-1470-5.

Kent, A. J., Darr, C., Koleszar, A. M., Salisbury, M. J., and Cooper, K. M. (2010) Preferential eruption of andesitic magmas through recharge filtering. Nature Geoscience, 3, 631. doi.org/10.1038/NGEO924.

Laumonier, M., Scaillet, B., Pichavant, M., Champallier, R., and Arbaret, L. (2014) On the conditions of magma mixing and its bearing on andesite production in the crust. Nature Communications, 5, 5607. doi.org/10.1038/ncomms6607.

Lee, C.T., and Bachmann, O. (2014) How important is the role of crystal fractionation in making intermediate magmas? Insights from Zr and P systematics. Earth and Planetary Science Letters, 393, 266–274. doi.org/10.1016/j.epsl.2014.02.044.

Li, N., Zhang, B., Danisik, M., Chen, Y. J., Selby, D., and Xiao, W. J. (2022) Multi-system chronometry to address preservation and exhumation of an Andean-type continental arc: Insights from the Paleozoic Axi epithermal deposit Chinese Western Tianshan. Journal of the Geological Society London, jgs2021-150.

Liu, X. X., Wang, G. H., Huo, Q., Xie, J. P., Li, S. P., Wu, H. Y., and Guo, Y. J. (2015) Novel two-step process to improve efficiency of bio-oxidation of Axi high-sulfur refractory gold concentrates. Transactions of Nonferrous Metals Society of China, 25, 4119–4125. doi.org/10.1016/S1003-6326(15)64063-8 (in Chinese with English abstract).

Liu, Z., Mao, X., Deng, H., Li, B., Zhang, S., Lai, J., Bayless, R. C., Pan, M., Li, L., and Shang, Q. (2018) Hydrothermal processes at the Axi epithermal Au deposit, western Tianshan: Insights from geochemical effects of alteration, mineralization and trace elements in pyrite. Ore Geology Reviews, 102, 368−385. doi.org/10.1016/j.oregeorev.2018.09.009.

Liu, Z., Mao, X., Ackerman, L., Li, B., Dick, J. M., Yu, M., Peng, J., and Shahzad, S. M. (2020) Two-stage gold mineralization of the Axi epithermal Au deposit, Western Tianshan, NW China: Evidence from Re–Os dating, S isotope, and trace elements of pyrite. Mineralium Deposita, 55, 863−880. doi.org/10.1007/s00126-019-00903-6.

Martin, A. J., Keith, M., Parvaz, D. B., McDonald, I., Boyce, A. J., McFall, K. A., Jenkin, G. R. T., Strauss, H., and MacLeod, C. J. (2020) Effects of magmatic volatile influx in mafic VMS hydrothermal systems: Evidence from the Troodos ophiolite, Cyprus. Chemical Geology, 531, 119325. doi.org/ 10.1016/j.chemgeo.2019.119325.

Murowchick, J.B. (1992) Marcasite inversion and the petrographic determination of pyrite ancestry. Economic Geology, 87, 1141−1152.

Mustard, R., Ulrich, T., Kamenetsky, V.S, Mernagh, T., 2006. Gold and metal enrichment in natural granitic melts during fractional crystallization. Geology, 34, 85−88. doi.org/10.1130/G22141.1.

Nadeau, O., Stix, J., and Williams-Jones, A. E. (2016) Links between arc volcanoes and porphyry-epithermal ore deposits. Geology, 44, 11–14. doi.org/10.1130/G37262.1.

Paton, C., Hellstrom, J., Paul, B., Woodhead, J., and Hergt, J. (2011) Iolite: Freeware for the visualisation and processing of mass spectrometric data. Journal of Analytical Atomic Spectrometry, 26, 12, 2508–2518. doi.org/10.1039/c1ja10172b.

Putnis, A. (2009) Mineral Replacement Reactions. Reviews in Mineralogy and Geochemistry, 70, 87–124. doi.org/10.2138/rmg.2009.70.3.

Reubi, O., and Blundy, J. (2009) A dearth of intermediate melts at subduction zone volcanoes and the petrogenesis of arc andesites. Nature, 461, 7268, 1269. doi.org/10.1038/nature08510.

Rudnick, R. L. (1995) Making continental crust. Nature, 378, 6557, 571–578. doi.org/10.1038/378571a0.

Rui, Z.Y., Goldfarb, R.J., Qiu, Y.M., Zhou, T.H., Chen, R.Y., Pirajno, F., and Yun, G. (2002) Paleozoic-early Mesozoic gold deposits of the Xinjiang Autonomous Region, northwestern China. Mineral Deposita, 37, 393–418. doi.org/10.1007/s00126-001-0243-6.

Seward, T., Williams-Jones, A.E, and Migdisov, A. (2014). The chemistry of metal transport and deposition by ore-forming hydrothermal fluids. Treatise on Geochemistry 2nd Edition, 29–57. doi.org/10.1016/B978-0-08-095975-7.01102-5

Sillitoe, R. H., and Hedenquist, J. W. (2003) Linkages between volcanotectonic settings, ore-fluid compositions, and epithermal precious metal deposits. Special Publication-Society of Economic Geologists, 10, 315–343. doi.org/ 10.1126/science.101.2621.295-b.

Simmons, S. F., and Brown, K. L. (2007) The flux of gold and related metals through a volcanic arc, Taupo Volcanic Zone, New Zealand. Geology, 35, 1099–1102. doi.org/ 10.1130/G24022A.1.

Simmons, S. F., White, N. C., and John, D. A. (2005) Geological characteristics of epithermal precious and base metal deposits. Economic Geology 100th anniversary volume, 29, 485–522. doi.org/10.2113/gsecongeo.100.5.1052.

Stern, C.R., Funk, J.A., Skewes, M.A., and Arevalo, A. (2007) Magmatic anhydrite in plutonic rocks at the El Teniente Cu-Mo deposit, Chile and the role of sulfur- and copper-rich magmas in its formation. Economic Geology, 102, 1335–1344. doi.org/10.2113/gsecongeo.102.7.1335.

Webster, J.D., and Botcharnikov, R.E. (2011) Distribution of sulfur between melt and fluid in S-O-H-C-Cl-bearing magmatic systems at shallow crustal pressures and temperatures. Reviews in Mineralogy and Geochemistry, 73, 247–283. doi.org/10.2138/rmg.2011.73.9

White N. C., and Hedenquist J. W. (1990) Epithermal environments and styles of mineralization - variations and their causes, and guidelines for exploration.

Journal of Geochemical Exploration, 36, 445–474. doi.org/10.1016/0375-6742(90)90063-G.

White N. C., and Hedenquist J. W. (1995) Epithermal gold deposits: styles, characteristics and exploration. Society of Economic Geology newsletter 23, 9–13.

Williams-Jones, A.E., and Heinrich, C.A. (2005) Vapor transport of metals and the formaiton of magmatic-hydrothermal ore deposits. Economic Geology, 100, 1287–1312. doi.org/10.2113/100.7.1287.

Williams-Jones, A.E., and Migdisov, A.A. (2014) Experimental constraints on the transport and deposition of metals in ore-forming hydrothermal systems. In: Kelley, K.D., and Golden, H.C. Builing Exploration Capability for the 21th Century. 18, 77–95.

Williams-Jones, A.E., Migdisov, A.A., Archibald, S.M., and Xiao, Z.F. (2002) Vapor-transport of ore metals. In: Hellmann, R., and Wood, S.A. Water-rock interactions, ore deposits, and environmental geochemsitry: A tribute to David A. Crerar. The Geologicla Society, specially publication, 7, 279–305.

Wood, S.A. and Samson, I.M. (1998) Solubility of ore minerals and complexation of ore metals in hydrothermal solutions. Reviews in Economic Geology, 10, 33–80.

Ye, T., Xi, W., Li, N., and Danisk, M. (2020). From magma replenishment to epithermal mineralization: Combined evidence from zircon U-Pb, (U-Th-[Sm])/He and trace element data. Ore Geology Reviews, doi.org/10.1016/j.oregeorev.2020.103746.

Yu, J., Li, N., Qi, N., Guo, J.P., and Chen, Y.J. (2018) Carboniferous-Permian tectonic transition envisaged in two magmatic episodes at the Kuruer Cu-Au deposit, Western Tianshan (NW China). Journal of Asian Earth Sciences, 153, 395–411. doi.org/ 10.1016/j.jseaes.2017.07.048.

Zajacz, Z., Halter, W.E., Pettke, T., and Guillong, M. (2008) Determination of fluid/melt partition coefficients by LA-ICPMS analysis of co-existing fluid and silicate melt inclusions: Controls on element partitioning. Geochmica et Cosmochimica Acta, 72, 2169-2197. doi.org/10.1016/j.gca.2008.01.034

Zajacz, Z., Candela, A., Piccoli, M., Waelle, M., and Sanchez-Valle, C. (2012) Gold and copper in volatile saturated mafic to intermediate magmas: Solubilities, partitioning, and implications for ore deposit formation. Geochimica et Cosmochimica Acta, 91, 140–159. doi.org/10.1016/j.gca.2012.05.033.

Zhai, W., Sun, X. M., Sun, W. D., Su, L. W., He, X. P., and Wu, Y. L. (2009) Geology, geochemistry, and genesis of Axi: A Paleozoic low-sulfidation type epithermal gold deposit in Xinjiang, China. Ore Geology Reviews, 36, 265–281. doi.org/10.1016/j.oregeorev.2009.04.003.

Zhang, B. (2020) Metallogeny study of the Axi gold deposit in Western Tianshan, Xinjiang. Ph.D. thesis, Peking University, Beijing, 229 p (in Chinese with English abstract).

Zhang, B., Li, N., Shu, S., Wang, W., Yu, J., Chen, X., Ye, T., and Chen, Y. (2018) Textural and compositional evolution of Au-hosting Fe-S-As minerals at the Axi epithermal gold deposit, Western Tianshan, NW China. Ore Geology Reviews, 100, 31–50. doi.org/10.1016/j.oregeorev.2017.08.002.

FIGURE CAPTIONS

FIGURE 1. A simplified geological map of the Axi epithermal deposit (modified after Zhang et al., 2018).

FIGURE 2. Representative SEM images, showing textures of different types of pyrite and marcasite.

A: Py1 characterized by a porous core (Py1a), a compact mantle (Py1b) and an oscillatory-zoned rim (Py1c). Near it is bladed Mar1 with an arsenopyrite overgrowth. Also shown is a laser ablation traverse across the crystal; B: Py2 accompanied by coeval chalcopyrite and tetrahedrite; C: tiny, oscillatory-zoned Py3; D. Mar2 with a laminated relict “core” (Mar2a), clear “rim” (Mar2b) and an arsenopyrite overgrowth; E. fan-shaped Mar3 (with an arsenopyrite overgrowth) coexisting with chalcedony and calcite; F. Homogeneous Mar4 characterized by the absence of an arsenopyrite overgrowth and coexistence with zoned calcite.

Abbreviations: Asp-arsenopyrite; Cc-calcite; Ccp-chalcopyrite; Mar-marcasite; Py-pyrite; Qz-quartz; Td-tetrahedrite.

FIGURE 3. Photomicrographs showing paragenetic relationship among different types of pyrite and marcasite.

A: Py1 crosscut by Mar1; B: pseudomorphic replacement of clinopyroxene by Py1; C: a breccia clast containing Py1 cemented by Py1+quartz; Py1 crystals at the reaction front or in the clast are morphologically irregular (Py1a), whereas those away from the front or in the cement are subhedral to euhedral Py1b or Py1c; D: Py1 included in or surrounded by Py2; E: Py2 crosscut by Mar3; F: Py1-bearing clast cemented by Py3+chalcedony; G: a clast containing Py1, Py3 and Mar1 cemented by Mar2; H: a calcite-Mar4 vein crosscutting a calcite-chalcedony-Mar3 vein; I: a lattice texture composed of platy quartz (pseudomorphs after calcite) and adularia, which was crosscut or infilled by later calcite. The yellow lines illustrate the inner textural boundary (A), and the white lines outline the phenocryst (B), breccia (C, F, G), or veinlet (H).

Mineral abbreviation: Adl-adularia; Apy-arsenopyrite; Cc-calcite; Cln-chalcedony; Mar-marcasite; Py-pyrite; Qz-quartz.

FIGURE 4. Crustiform banding characterized by the rhythmic alternation of quartz, chalcedony, Py3 and Mar1.

The crustiform bands comprise eight thin layers (numbered 1 to 8); Mar 1 either forms thin laminae (layer 7 in Fig. C)) alternating with aggregates of Py3 and chalcedony (layer 1), or coexist with Py3 and arsenopyrite in a single band, indicating nearly contemporaneous precipitation of Mar1 and Py3.

Mineral abbreviation: Apy-arsenopyrite; Mar-marcasite; Py-pyrite.

FIGURE 5. Boxplots of selected trace element concentrations in pyrite and marcasite, illustrating the episodic nature of the gold mineralizing events (Au1, Au2, Au3) and Ag-Pb-Zn-Sb enrichment (BM1, BM2, BM3).

FIGURE 6. Two laser ablation traverses across a Py1 grain illustrating the elevated Au and As contents of Py1b. There are numerous inclusions (e.g., rutile and galena) in the core (Py1a).

FIGURE 7. A schematic model showing the relationship between mafic magma replenishment, magmatic degassing, sulfide precipitation and mineralization.

Fig. A shows intense magmatic degassing associated with the intrusion of mafic magma into a shallow, felsic magma reservoir, where the degassed, supercritical volatile is enriched in Au, As and S. Fig. B illustrates a period of magma quiescence, during which the magma and exsolved supercritical fluids are gradually enriched in Ag, Cu, Pb, Zn and Sb. During intrusion of the mafic magma, the supercritical fluid is vapor-like and condenses brine, with S, Au and As transported dominantly by the vapor before injection into circulating meteoric water, whereas during magma

DOI: https://doi.org/10.2138/am-2022-8610. http://www.minsocam.org/

quiescence the temperature is lower, the supercritical fluid is liquid-like and Cl, Cu, Ag, Pb, Zn are transported by the brine.

Fig. C illustrates the association between magma degassing and precipitation of FeS_2. The formation of porous, Co-Ni-V-Cr-Ti-rich Py1a and Mar2a was caused by coupled dissolution-reprecipitation of the host andesite (here represented by the clinopyroxene, i.e. Cpx). The incursion of Au-As-S-rich volatile induced precipitation of Py1b, Py3 and Mar3, while the Ag-Cu-Pb-Zn-Cd-rich volatile favored formation of Py2, Mar2b and Mar4. Interlayered Mar1 with Py3 in crustiform banding resulted from mixing with (or diluted by) meteoric water.

TABLE CAPTIONS

Table 1 Summary of compositions of pyrite and marcasite from the Axi gold deposit (ppm)

Appendix

Appendix A1. Composition and reproducibility of the standard MASS-1.

Appendix A2. Compositions of selected pyrite and marcasite crystals from the Axi gold deposit (ppm).

This is the peer-reviewed, final accepted version for American Mineralogist, published by the Mineralogical Society of America.
The published version is subject to change. Cite as Authors (Year) Title. American Mineralogist, in press.
DOI: https://doi.org/10.2138/am-2022-8610. http://www.minsocam.org/

Table 1. Summary of compositions of pyrite and marcasite from the Axi gold deposit (ppm)

No.	Hg	Au	Sb	Ag	Mo	Se	As	Zn	Cu	Co	Mn	Cr	V	Cs	Tl	Pb	Sc	Ti	Ni	Al
Py1a																				
Min.	0.08	1.3	47	6.3	0.04	4.4	9400	0.60	258	6.8	5.4	0.93	1.5	0.83	7.3	108	2.9	306	63	117
Max.	6.2	129	1160	95	27	17000	66300	37	2070	690	336	32	820	50	244	2550	50	38700	1400	17900
Med.	1.5	23	168	27	0.77	70	44000	9.6	459	209	28	12	14	10	43	381	11	3300	510	3860
Std.	2.2	35	276	22	7.6	4198	15257	9.3	370	159	83	8.0	168	11	67	627	13	7279	376	4537
Py1b																				
Min.	0.32	1.0	44	6.2	0.26	15	18900	0.20	56	0.61	0.80	0.24	0.37	0.32	0.16	2.3	0.09	8.3	3.9	2.5
Max.	4.4	147	2070	70	14	44000	168000	23	790	326	1600	34	1630	88	570	1090	36	18300	500	11200
Med.	1.2	39	107	23	1.5	195	67500	1.8	265	25	7.3	3.5	0.83	1.3	1.8	25	0.22	12	35	175
Std.	1.6	58	682	20	4.5	19149	48377	7.5	244	101	521	10	511	30	182	335	13	5745	148	4491
Py1c																				
Min.	0.03	1.0	11	1.5	0.02	1.10	3010	0.25	0.75	0.05	0.19	0.25	0.04	0.01	0.47	0.06	0.01	4.1	0.05	1.0
Max.	2.8	137	702	253	276	104	84300	2330	1710	570	202	266	164	5.7	125	3190	37	27000	936	32000
Med.	0.20	13	119	27	2.7	11	15000	1.1	96	11.0	4.9	1.0	0.67	1.0	8.0	30	0.16	7.7	40	153
Std.	0.57	35	138	44	43	18	17816	356	416	100	31	45	26	1.3	22	506	7.1	4453	206	5241
Py2																				
Min.	0.10	1.0	156	53	0.02	0.3	1890	20	296	0.74	0.42	0.18	0.04	0.02	6.2	6.3	0.01	4.2	5.3	0.40
Max.	0.45	15	2700	305	1.4	27	9600	1620	10200	221	11	6.8	6.3	2.1	39	521	0.17	270	242	1160
Med.	0.25	6.0	884	157	0.28	5.2	4610	96	928	38	2.4	0.64	0.59	0.53	18	124	0.07	5.3	66	341
Std.	0.08	3.3	596	86	0.38	6.1	1582	402	2388	51	2.4	1.5	1.6	0.59	9.8	117	0.05	77	69	326
Py3																				
Min.	0.20	0.17	10	0.04	0.02	6.0	5340	1.5	5.2	0.21	1.0	0.80	0.30	0.64	0.40	1.3	0.10	1.30	7.3	4.5
Max.	6.2	129	1590	330	10	650	142000	73	729	715	590	205	232	15	134	3300	75	95000	1660	62000

Med.	0.60	34	189	53	1.1	40	37100	9.7	292	106	27	15	11	6.2	34	306	3.9	1905	238	4175
Std.	1.8	37	375	59	3.4	166	31994	14	213	162	105	44	52	4.8	30	752	16	21683	482	12864
Mar1																				
Min.	0.03	4.1	44	20	8.2	1.9	3820	0.38	4.5	0.22	0.70	0.35	0.11	0.01	5.2	2.7	0.01	4.1	3.3	28
Max.	1.8	24	338	117	368	14	12700	3.7	186	41	6.5	14	3.1	1.7	27	374	1.8	14	527	1770
Med.	0.45	8.3	206	66	37	9.7	9555	0.64	18	6.4	1.6	0.89	0.91	0.67	15	13	0.66	5.4	168	336
Std.	0.54	5.7	82	27	114	3.3	2632	0.94	64	12	1.6	3.9	0.98	0.45	6.4	116	0.60	2.7	162	579
Mar2a																				
Min.	0.52	2.7	135	89	1.2	0.8	2120	2.1	35	11	0.42	0.47	1.0	0.23	3.4	6.0	1.0	4.9	186	5.7
Max.	12	16	1169	350	83	3200	29500	219	225	841	5090	215	39	9.0	461	840	38	180	2440	8000
Med.	4.4	5.3	581	243	3.7	4.5	6380	69	139	298	1190	8.0	9.7	0.68	71	206	12	32	697	205
Std.	3.2	2.7	261	72	22	1049	8566	61	42	182	1374	67	8.3	3.2	135	235	12	56	701	1914
Mar2b																				
Min.	0.36	0.18	48	9.9	0.19	2.8	15	0.43	11	0.91	2.0	0.96	0.20	0.11	5.6	0.22	0.03	4.1	2.2	3.6
Max.	5.3	19	1430	253	65	1300	52600	532	980	313	19400	66	189	5.7	402	361	133	160	2530	18800
Med.	1.5	4.0	190	60	6.0	8.0	3235	27	71	58	43	3.8	7.0	1.3	62	38	2.2	13	195	410
Std.	1.4	5.4	272	54	16	503	10791	143	195	79	3906	17	43	1.7	91	91	32	50	533	3710
Mar3																				
Min.	1.3	4.4	348	77	0.40	1.1	8300	0.90	95	150	4.0	1.7	0.50	0.08	16	47	0.13	7.2	359	48
Max.	10	34	2710	369	5.2	180	94300	1510	357	2870	14500	40	59	9.1	92	2370	92	150	8430	41900
Med.	2.6	12	872	146	1.4	20	25400	29	138	290	1030	16	7.7	2.9	56	169	9.7	30	1460	5700
Std.	3.0	7.2	610	63	1.1	44	22709	366	66	634	4139	9.8	14	2.6	21	554	25	37	1747	10101
Mar4																				
Min.	8.4	0.07	325	8.5	1.4	1.6	2500	52	563	401	189	1.3	0.86	0.08	17	619	0.23	5.7	158	32
Max.	15	0.19	797	15	4.9	12	4450	341	2900	955	3560	189	44	3.5	40	1252	29	830	407	15600
Med.	13	0.11	417	13	2.6	5.8	3115	104	779	706	1056	8.2	15	0.68	29	1027	6.7	7.2	258	114

Std.	2.1	0.03	126	2.2	0.87	3.1	566	67	546	152	990	49	14	1.0	6.4	190	10	199	64	3737

This is the peer-reviewed, final accepted version for American Mineralogist, published by the Mineralogical Society of America.
The published version is subject to change. Cite as Authors (Year) Title. American Mineralogist, in press.
DOI: https://doi.org/10.2138/am-2022-8610. http://www.minsocam.org/

Fig. 1

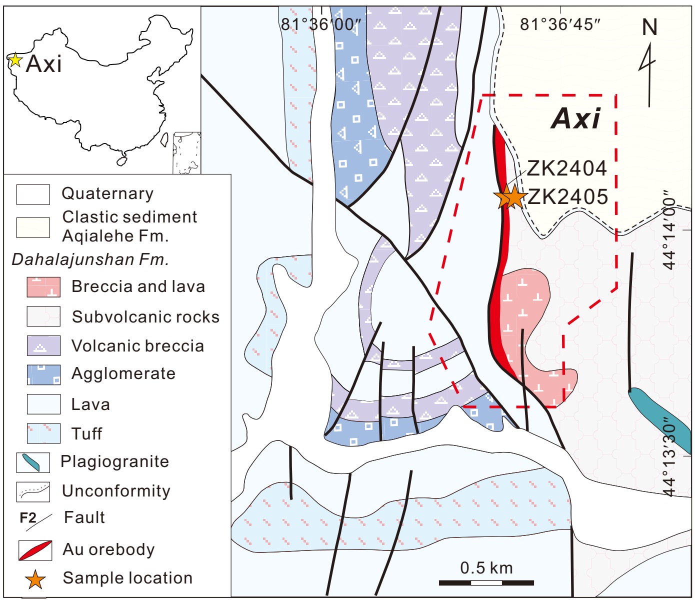

This is the peer-reviewed, final accepted version for American Mineralogist, published by the Mineralogical Society of America.
The published version is subject to change. Cite as Authors (Year) Title. American Mineralogist, in press.
DOI: https://doi.org/10.2138/am-2022-8610. http://www.minsocam.org/

Fig. 2

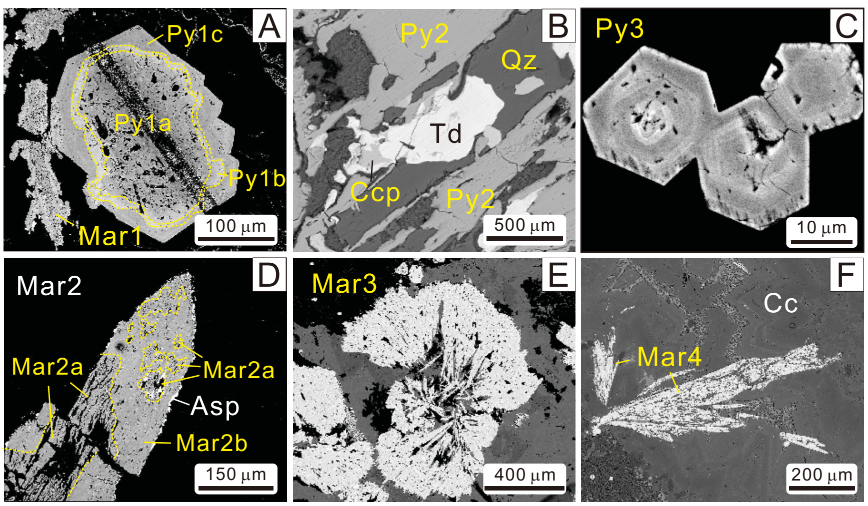

This is the peer-reviewed, final accepted version for American Mineralogist, published by the Mineralogical Society of America.
The published version is subject to change. Cite as Authors (Year) Title. American Mineralogist, in press.
DOI: https://doi.org/10.2138/am-2022-8610. http://www.minsocam.org/

Fig. 3

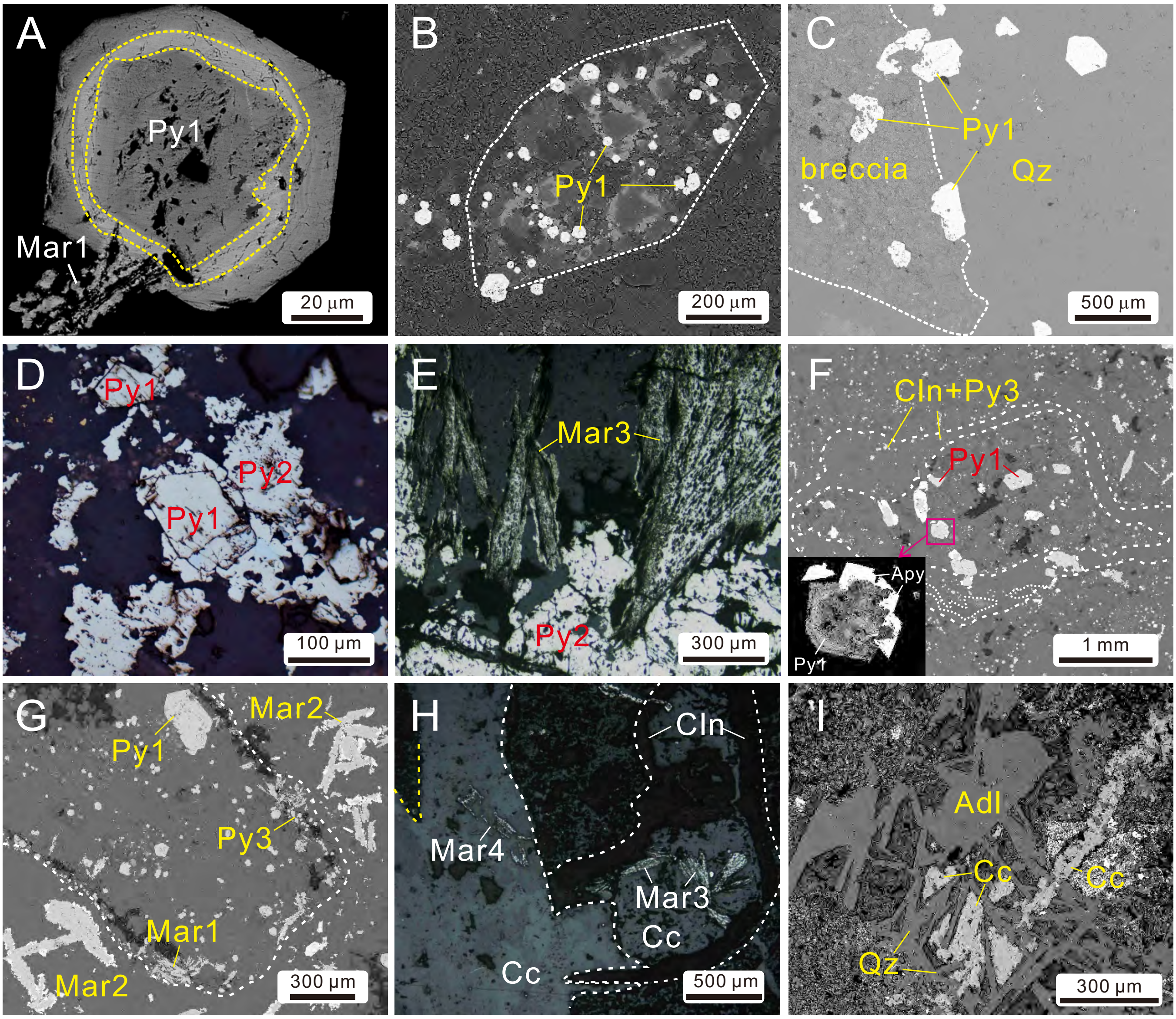

This is the peer-reviewed, final accepted version for American Mineralogist, published by the Mineralogical Society of America.
The published version is subject to change. Cite as Authors (Year) Title. American Mineralogist, in press.
DOI: https://doi.org/10.2138/am-2022-8610. http://www.minsocam.org/

Fig. 4

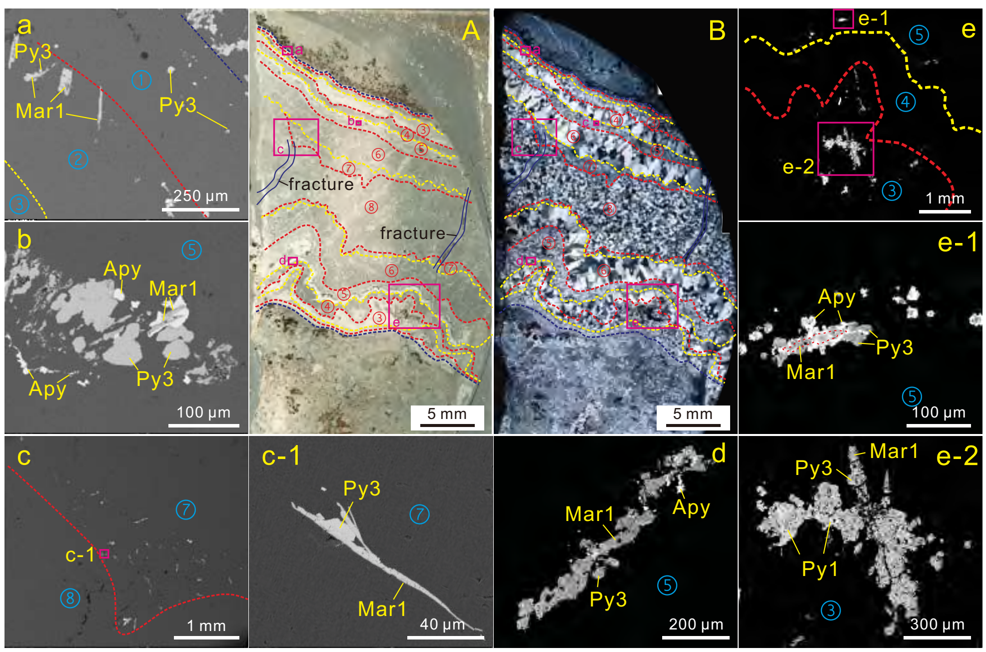

DOI: https://doi.org/10.2138/am-2022-8610. http://www.minsocam.org/

Fig.5

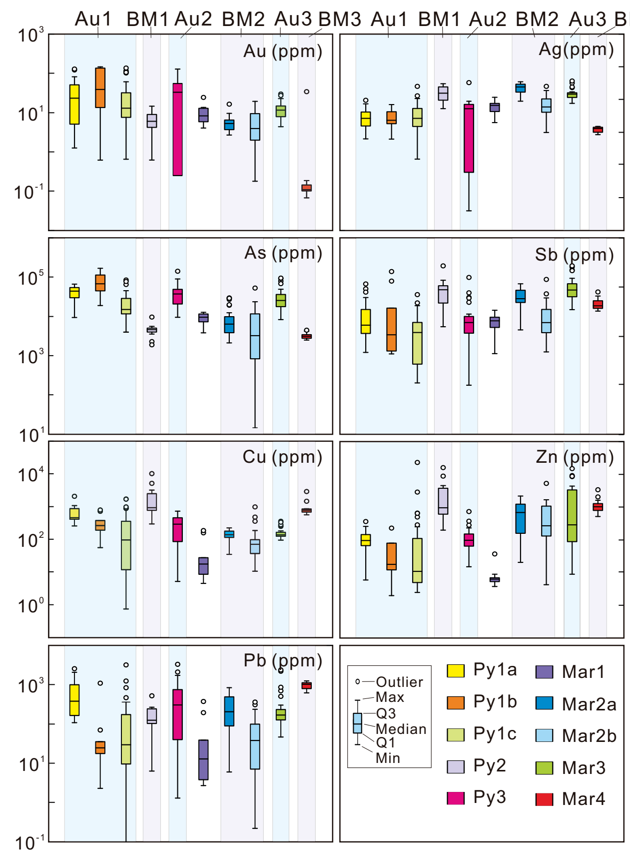

DOI: https://doi.org/10.2138/am-2022-8610. http://www.minsocam.org/

Fig.6

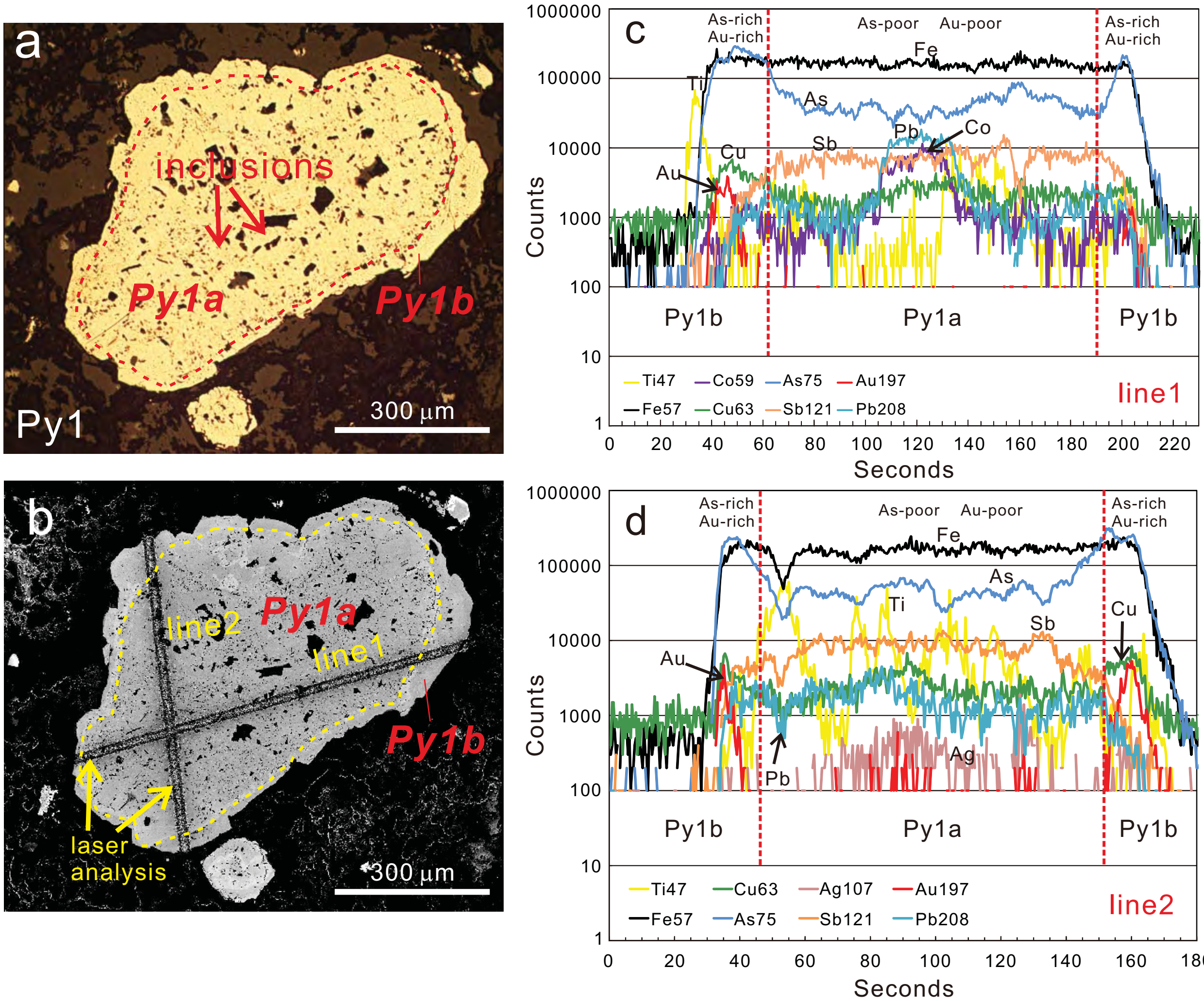

DOI: https://doi.org/10.2138/am-2022-8610. http://www.minsocam.org/

Fig.7